Synchrotron radiography of Richtmyer–Meshkov instability driven by exploding wire arrays

View Online   Export Citation   CrossMark

J. Strucka,[1,a] B. Lukic,[2] M. Koerner,[1] J. W. D. Halliday,[1] Y. Yao,[1] K. Mughal,[1] D. Maler,[3] S. Efimov,[3] J. Skidmore,[4] A. Rack,[2] Y. Krasik,[3] J. Chittenden,[1] and S. N. Bland[1]

AFFILIATIONS

[1]Plasma Physics Group, Imperial College London, London SW7 2BW, United Kingdom
[2]European Synchrotron Radiation Facility, CS 40220, 38043 Grenoble Cedex 9, France
[3]Physics Department, Technion–Israel Institute of Technology, Haifa 32000, Israel
[4]First Light Fusion Ltd., Unit 10 Oxford Industrial Park, Mead Road, Yarnton, Oxfordshire OX5 1QU, United Kingdom

Note: This paper is part of the special topic, Shock Waves.
[a]Author to whom correspondence should be addressed: jergus.strucka15@imperial.ac.uk

ABSTRACT

We present a new technique for the investigation of shock-driven hydrodynamic phenomena in gases, liquids, and solids in arbitrary geometries. The technique consists of a pulsed power-driven resistive wire array explosion in combination with multi-MHz synchrotron radiography. Compared to commonly used techniques, it offers multiple advantages: (1) the shockwave geometry can be shaped to the requirements of the experiment, (2) the pressure ($P > 300$ MPa) generated by the exploding wires enables the use of liquid and solid hydrodynamic targets with well-characterized initial conditions (ICs), (3) the multi-MHz radiography enables data acquisition to occur within a single experiment, eliminating uncertainties regarding repeatability of the ICs and subsequent dynamics, and (4) the radiographic measurements enable estimation of compression ratios from the x-ray attenuation. In addition, the use of a synchrotron x-ray source allows the hydrodynamic samples to be volumetrically characterized at a high spatial resolution with synchrotron-based microtomography. This experimental technique is demonstrated by performing a planar Richtmyer–Meshkov instability (RMI) experiment on an aerogel–water interface characterized by Atwood number $A_0 \sim -0.8$ and Mach number $M \sim 1.5$. The qualitative and quantitative features of the experiment are discussed, including the energy deposition into the exploding wires, shockwave generation, compression of the interface, startup phase of the instability, and asymptotic growth consistent with Richtmyer's impulsive theory. Additional effects unique to liquids and solids—such as cavitation bubbles caused by rarefaction flows or initial jetting due to small perturbations—are observed. It is also demonstrated that the technique is not shape dependent by driving a cylindrically convergent RMI experiment.

I. INTRODUCTION

Hydrodynamic instabilities are of fundamental importance to geophysical and astrophysical flows,[1,2] planetary sciences,[3] inertial confinement fusion,[4] and other applications.[5–8] The Richtmyer–Meshkov instability (RMI) describes the baroclinic vorticity deposition that occurs during an impulsive acceleration of an interface separating fluids of different densities—usually due to the passage of a shockwave—and the resulting dynamics lead to the amplification of any perturbation on the interface. This process, unlike the Rayleigh–Taylor instability, can be realized in both light–heavy and heavy–light configurations. In its nonlinear stage, the RMI tends to form a turbulent mixing layer through its interaction with the Kelvin–Helmholtz instability. Due to the ubiquity of this phenomenon, it is interesting to understand the dependence of the fluid mixing initiated by the RMI on the initial conditions (ICs) of the interface.

Recent theoretical and numerical studies[9–15] have broadly focused on understanding the effect of two different types of ICs. In the first case, the RMI induced by a shock passing an arbitrary shaped interface was considered and shown to significantly affect the initial vorticity deposition and growth speed.[9,10] A corollary of this research was the optimization of the initial shape of the interface to suppress the RMI.[11] The second type of ICs—consisting of small broadband perturbations deposited on the interface by stochastic or manufacturing processes—was considered in connection to the persistence

memory of the ICs in the nonlinear turbulent stage.[6] Numerical simulations in both two (2D) and three (3D) dimensions show that the growth rate exponent θ of the turbulent mixing layer, as well as the mixing fraction, is strongly dependent on the ICs described by broadband and narrowband power spectra.[13]

Experimental investigations have focused on the first type of ICs, understanding the effect of the interface shape—likely due to its easier experimental diagnostics. The experiments mainly used shock tubes with initially separated gases (usually N_2 and SF_6). Example investigations include the shock interaction with a rectangular block,[16] cylinder,[17] two cylinders,[18] inclined interfaces,[19–22] thin curtains,[23] and many other experimental configurations. The separation of the gas species in these experiments was achieved with a thin shaped nitrocellulose membrane, or with a gravity-assisted flow for membrane-less experiments.[24,25] The disadvantage of the former method is the potential disruption of the flow by the fragments of the membrane, while the latter suffers from the production of a diffusion layer that inhibits the RMI[26]—both effects changing the ICs. Experiments with broadband ICs were largely conducted with statistically repeatable shear-flow experiments.[27–29]

More recently, RMI experiments utilized platforms traditionally used to study matter at extreme conditions (temperature $T > 1$ eV, pressure $P > 1$ Mbar), such as high-powered lasers[30] or magnetically driven pulsed power.[31] The extreme pressures (pressure $\gg$ yield strength) and shock speeds (Mach number $M > 10$) generated by these drivers allow manufacture of hydrodynamic targets from solid materials with a well-characterized initial topology. The experiments investigated the single-mode RMI growth at high values of M in planar,[32] cylindrical,[30,31] and thin-layer configurations.[33] Despite the well-known ICs in these experiments, the fast shock speeds make it a challenge to obtain more than 1–2 radiographs per experiment and require repeating experiments with the same ICs to measure the growth over time. At the same time, the solid targets and convergent geometries often employed in these systems lead to optical opacity and a requirement for x-ray diagnostics.

In this article, we present a novel platform for RMI experiments in arbitrary geometries using the underwater electrical wire explosion (UEWE). UEWE occurs when a current pulse with duration in the range of 10^{-7}–10^{-6} s and the current density of $>10^7$ A/cm^2 dynamically heats and explodes an array of thin metallic wires submerged in water. As the wires explode, they drive a strong shock traveling at multi-km s^{-1} speeds and multi-kbar pressures into the surrounding medium.[34,35] The shock geometry can be adjusted to the requirement of the experiment by changing the wire array geometry. Previous research has explored planar,[36,37] cylindrical,[38,39] and spherical shockwave production.[40] Unlike the name suggests, the UEWE does not necessitate the use of water and can be successfully performed in any dielectric medium, including plastics and epoxy resins.[41] Similar approaches were also used to explore shock interaction with water columns[42] or reservoir stimulation.[43]

In this article, we describe a proof-of-concept RMI experiment conducted on the pulsed power driver (PPD) located at the European Synchrotron Research Facility Microtomography beamline (ID19). The combination of the PPD and the multi-frame synchrotron radiography enables measurement of up to 256 radiographs (60 ps exposure) per experiment in arbitrary geometries, including convergent geometries usually inaccessible to visible light. It opens the possibility of observing the development of the RMI in a single experiment, arbitrary geometry, and with well-characterized ICs.

The remainder of the article is organized as follows: in Sec. II, we describe the experimental setup, including details of the pulsed power generator, wire arrays, and x-ray diagnostics. In Sec. III, we detail the reasoning behind the choice of our hydrodynamic target and its pre-shot characterization. In Sec. IV, we show the results of an example RMI experiment and describe the observed dynamics. Finally, in Sec. V, we discuss the implications of this work and future research avenues.

II. EXPERIMENTAL SETUP AND DIAGNOSTICS
A. Electrical setup and diagnostics

The electrical setup consisted of a compact pulsed power generator with four 0.22 μf Maxwell capacitors connected in parallel and discharged through an externally triggered pancake spark gap switch. The spark gap switch was connected to the electrical load and triggered by a pulse provided by a PT-55 spiral generator. The high voltage trigger pulse was essential to lower the timing jitter of the system to <10 ns, a timing accuracy required for reliable co-timing with experimental diagnostics, such as multi-MHz synchrotron radiography or streak cameras. On each shot, the capacitors were charged to $+30$ kV (stored energy ~400 J). The discharge current was measured by a self-integrating Rogowski coil placed at the output of the generator and a current-viewing resistor (CVR) placed at the output of the load as shown in Fig. 1(a). The voltage was measured by a P6015A Tektronix voltage divider connected across the load. Additional details of the pulsed power setup were discussed in an earlier publication.[44]

B. Wire array load and experimental geometry

The experimental cell consisted of a wire array and the hydrodynamic target enclosed within a 50 mm diameter cylindrical plastic capsule filled with water. During the experiments, the chamber was filled with de-ionized water for two purposes. First, the de-ionized water prevented formation of a plasma channel along the wire surface and tamped the wire expansion, thus maintaining high energy density deposition into the wire material by localizing the current flow and maintaining high resistivity for a longer time. Second, the de-ionized water served as the working fluid into which the exploding wires launched shocks, which were used to drive the hydrodynamic experiments.

In Fig. 1(b), we show the load geometry used in the presented research: a planar wire array consisting of 19 copper wires of 64 μm diameter spaced 0.8 mm apart. The wires were connected to the high voltage electrode and grounded through the CVR. The number of wires and their spacing was chosen to produce a planar shockwave. At a propagation distance >2 mm from the initial wire array position, numerical simulations of the shockwave performed in the magnetohydrodynamic code GORGON suggest a water density variation $<0.5\%$ in the leading mm of the shockwave. The width of the array was chosen such that the resulting planar shockwave spanned the entire experimental field-of-view shown in Fig. 1(b) (red dotted rectangle). The total cross section of the wires and the wire length were optimized to maximize the energy density deposition rate into the wire material, which is realized for close to critically damped (slightly overdamped) discharge and results in stronger shockwave generation due to faster radial expansion of wires.[45]
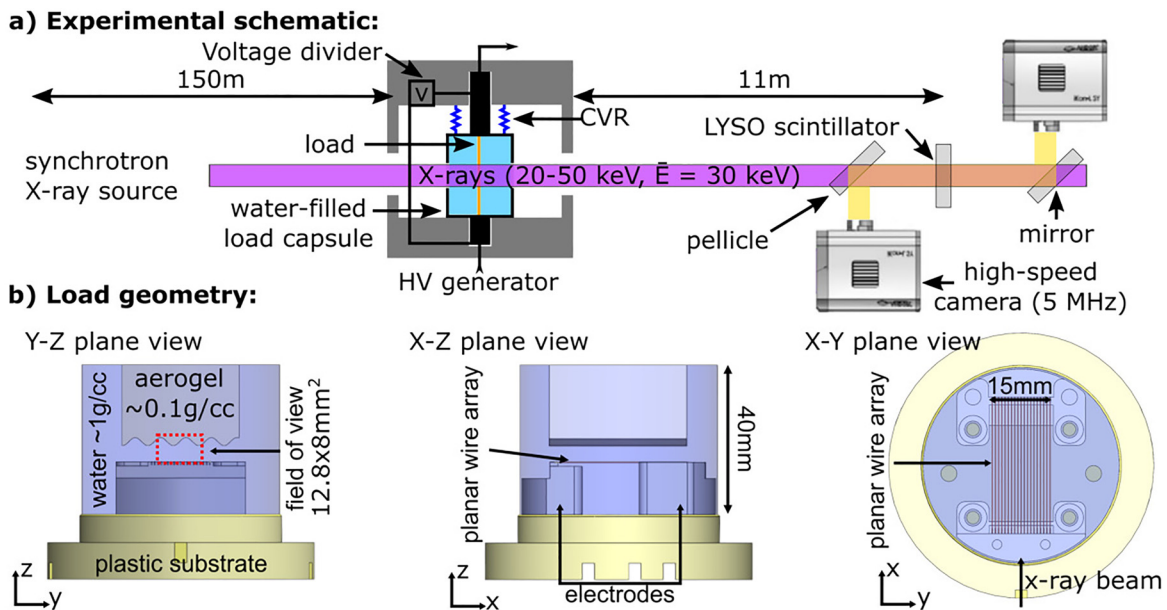
FIG. 1. (a) The experimental setup. (b) The geometry of the experimental load used in the present research.

The cross section of wires, which determines the time of the wire explosion (i.e., when the vapor-low-ionized plasma phase transition occurs), was estimated using tabulated values of the current action integral for copper.[46] Here, we consider the time of explosion τ_{ex} to be $\tau_{ex} = 1.41(LC)^{1/2}$, where L and C are the total inductance and capacitance of the discharge circuit. The condition for the coincidence of peak current with the explosion time in terms of the current action integral $\bar{h}$ is $\tau_{ex} \approx 2\bar{h}/j^2$, where j is the current density per unit area and $\bar{h}$ is a tabulated value that primarily depends on the wire material for sufficiently fast discharges. In our experiments, the specific current action integral at peak voltage (corresponding to wire explosion) was 2×10^9 A^{2}s/cm^4 compared to the tabulated value of 2–4×10^9 A^{2}s/cm^4,[46] suggesting optimal wire explosion parameters for high energy density deposition. The length of the wires was 35 mm, adjusted empirically until the current pulse became almost critically damped, as shown in Fig. 2.

An example of the current and resistive voltage waveforms measured in a typical experiment is shown in Fig. 2. The current waveform was measured by the CVR, while the resistive voltage waveform was calculated by subtracting the inductive voltage $L_l dI/dt$ from the measured voltage, where L_l is the load inductance. The discharge was characterized by a peak current density of $j \sim 5 \times 10^{11}$ A/m^2 through the wire cross section. The skin depth of the discharge at standard conditions was $\delta \sim 130\,\mu m$, which is ~ 4 times larger than the radius of the wires, implying uniform current distribution and energy deposition throughout the wire volume. The resistive voltage reached a maximum of ~ 40 kV approximately 300 ns after peak current. At the time of explosion, the corresponding deposited energy $\int I(t)V_R(t)dt$ in the wire material was ~ 300 J, showing a total efficiency in energy deposition of 75% in the first 1.5 μs of the discharge.

C. Ultra-fast x-ray imaging

The main diagnostic in these experiments was multi-MHz x-ray radiography. Using x-ray imaging enables the use of optically opaque samples, such as foams, plastics, or low Z metals, as well as experiments in convergent geometries where the compression geometry does not allow a direct line of sight and obscures the dynamics—e.g., spherical geometry or side-on imaging of cylindrical geometries. In addition, it is possible to estimate approximate mass densities from the
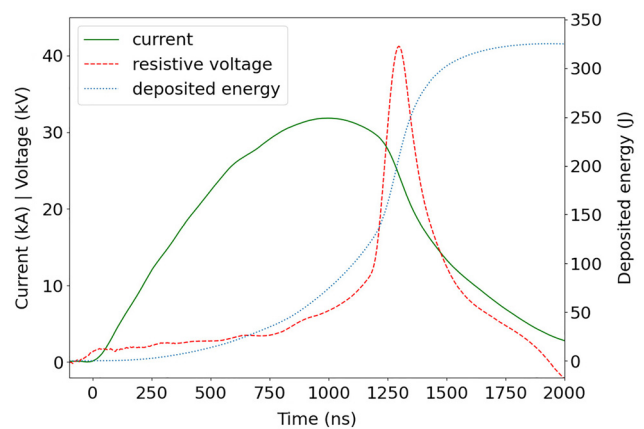

FIG. 2. Example of a typical current (solid green), resistive voltage (dashed red), and deposited energy (dotted blue) waveforms measured in an experiment. Most of the resistive energy deposition occurs during the wire explosion ($t \sim 1300$ ns) at peak resistive voltage.

obtained x-ray radiographs through attenuation measurements. The x-ray imaging was performed by a polychromatic synchrotron beam produced by two axially aligned long-period undulators ($\lambda = 32$ mm), with its harmonics spanning energies between 20 and 50 keV and a mean energy of $\bar{E} \sim 30$ keV.

During the experiments, the synchrotron storage ring operated in a 16-bunch filling mode (60 mA current) and delivered a photon flux of approximately 2×10^7 photons/mm^2 in a single 60 ps long pulse every 176 ns. After propagating through the experimental volume, the x rays were converted to visible light by a fast single-crystal scintillator (LYSO:Ce, 40 ns decay time, Hilger Crystals, UK) as shown in Fig. 1(a). The resulting light was lens-coupled via pellicle beamsplitters to two high-speed cameras (HPV-X2, Shimadzu Corp., Japan). The cameras operated with an inter-frame time of 200 ns and an exposure time of 100 ns captured 128 frames each and were triggered in parallel to capture every synchrotron pulse (delay of 100 ns between camera triggers). If the cameras were set to trigger in series (one after another), the time window of the measurement would be doubled to 50 μs at the cost of missing a single synchrotron x-ray pulse every ~ 1.3 μs due to the mismatch between the camera acquisition frequency and the radio frequency of the storage ring. It is important to remark that the temporal resolution of this single-bunch imaging was set by the 60 ps long x-ray pulse, not the 100 ns camera exposure.

The spatial resolution of the measurement was set to 32 μm/pixel by the pixel size of the cameras and magnification of the camera optics, giving a field-of-view of 8×12.8 mm^2 (V $\times$ H).

To visualize complex hydrodynamic flows, the x rays propagated 11 m past the target, reaching the "edge-enhancement mode" of phase-contrast imaging at the detector, i.e., propagation-based inline phase-contrast imaging[47] (source coherence length $d_t \sim 100$ μm). In this mode, interfaces between materials with different refraction indices are highlighted, while the bulk material density can still be analyzed assuming absorption-dominated radiography. More details about the imaging system can be found in previous publications.[48–51] In addition to the visualization, the x-ray radiographs were used to estimate mass densities of the samples during their hydrodynamic evolution via their x-ray absorption. Assuming linear response of the x-ray scintillator and the high-speed camera, the intensity of the x-ray beam after propagating through the water-filled capsule/sample was approximated by the Beer–Lambert law, $I = I_0 \exp(-\kappa \rho x)$, where I_0 is the initial intensity of the x-ray beam, κ is the attenuation coefficient of the sample for a given photon energy, ρ is the sample density, and x is the thickness of the sample along the line-of-sight. In earlier research,[36] we estimated the effective attenuation coefficient for a water target of the same thickness to be approximately equal to the mass attenuation of water at 40 keV. The representative energy of 40 keV used to approximate the polychromatic beam is higher than the mean beam energy. This is due to the more effective attenuation of lower energy photons by the water in the sample, hence contributing less to the transmitted beam: an effect which is well-known as "beam hardening" in microtomography with polychromatic illumination.

III. TARGET MANUFACTURE AND CHARACTERIZATION
A. Hydrodynamic target

To perform a successful hydrodynamic experiment, the target material needs to satisfy a set of requirements. First, the material must be machinable into a sample with a characteristic size of ~ 10 mm and

geometric perturbations on its interface with size ~ 200 μm. Second, the target should not chemically interact with water and should maintain its density while submerged. Finally, the yield compressive strength of the target needs to be orders of magnitude lower than the shock pressure for the non-hydrodynamic part of the pressure tensor to be negligible.

Polyurea aerogels are mechanically robust with a compressive yield strength between 0.6 and 13 MPa (much lower than the ~ 300 MPa of the shock pressure generated by our approach), do not soak water, have a discernible foam microstructure only on ~ 100 nm length scales,[52] and can be manufactured in the density range of 0.016–0.55 g/cm^3. These properties make polyurea aerogels perfect hydrodynamic targets as they can be fabricated into a variety of shapes prior to experiments. Recently, research at MIT, LANL, and AWE ascertained the equation-of-state and Hugoniot for the polyurea aerogel in multi-shock experiments.[52–54]

In our experiments, a commercially available polyurea aerogel was machined on a 3-axis CNC machine using a set of solid carbide end mills with 0.5 mm corner radii to obtain a sinusoidal perturbation on its interface. The machining of the sample was enabled by the compressive yield strength $Y \sim 0.6$ MPa at a low mass density of only 0.1 ± 0.02 g/cm^3 [Ref. 62]. Each target was machined from a $30 \times 20 \times 15$ mm^3 block with the transverse size (20 mm) larger than the field-of-view and the longitudinal size (30 mm) comparable to the wire length to minimize edge effects and increase the integrated x-ray attenuation along the line-of-sight.

B. Target characterization

To ascertain the ICs on the surface and within the aerogel volume, the samples were scanned using synchrotron-based microtomography prior to the experiments. A filtered pink beam generated by a wiggler insertion device (filters: 1.8 mm Diamond, 2.8 mm Aluminum, 0.14 mm Copper) with ~ 30 keV peak energy was used to illuminate the sample. The x-ray transmission and contrast were comparable to that used during the ultra-fast *in situ* measurements. For these measurements, an indirect x-ray detector was placed 1 m downstream from the sample to form propagation-based phase contrast on the air–aerogel interface. The indirect detector assembly consisted of a 500 μm LuAG:Ce scintillator optically coupled to a PCO Edge 5.5 detector. The resulting radiographs were 16.64×7.46 mm^2 (V $\times$ H) in size with a pixel size of 6.5 μm. The tomography scans were performed over 360°, capturing 2200 projections in total. The direct phase retrieval algorithm[55] was used to treat the projections prior to tomographic reconstruction that was carried out with the filtered back-projection algorithm using the Nabu software.[56] The reconstructed volumes were post-processed for ring removal using a set of in-house developed codes.

An example of a single 2D slice of such scan is shown in Fig. 3. The scan was performed over a volume of $16.64 \times 16.64 \times 16.64$ mm^3 with a voxel size of 6.5 μm^3. The sample was volumetrically homogeneous on the spatial scale of the scan. The Fourier transform of the aerogel surface exhibited undesired multimode perturbations of $< a_0/60$ amplitude in the $\lambda < 400$ μm space, where a_0 is the initial amplitude of the pre-imposed sinusoidal perturbation and λ is the wavelength. In principle, the standardization of the sample could be improved to sub-μm resolutions over longer scanning times to inform more highly resolved numerical simulations.
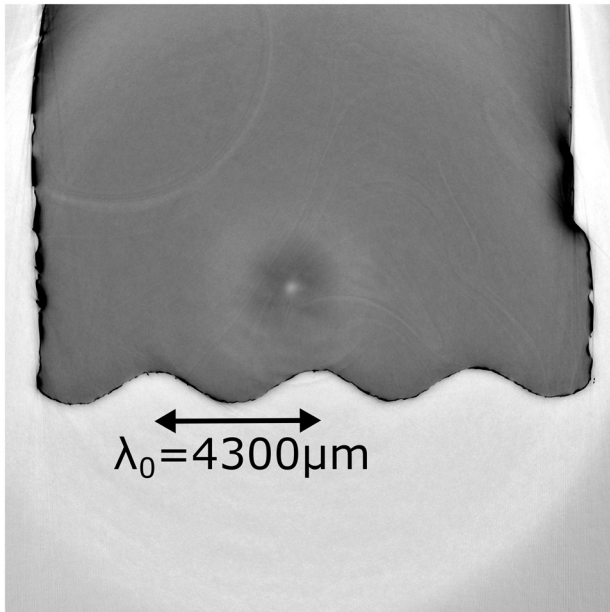
FIG. 3. A single 2D slice of a 3D synchrotron-tomography of an aerogel sample ($\lambda_0 = 4300\,\mu m$, $a_0/\lambda_0 \sim 0.2$) obtained prior to an experiment. Bright regions correspond to low x-ray attenuation (low density), while darker regions correspond to higher densities. The air–aerogel interface is highlighted via x-ray phase contrast imaging and shows high-frequency low-amplitude perturbations characteristic of all manufactured samples.

IV. RESULTS AND DISCUSSION

In this section, we present the results of an experiment measuring the single-mode planar RMI in the small amplitude regime. This well-established test problem serves to benchmark and highlight the capabilities offered by the presented experimental method.

We remind the reader of Fig. 1(b), where the conceptual design of the experiment including the field-of-view (highlighted in a red dashed rectangle) is shown. In Fig. 4, we show a small selection of radiographs obtained in a single experiment. The radiographs show the development of a sinusoidal interface ($\lambda_0 = 4.4$, $a_0 = 0.2$ mm) separating the water (1 g/cm^3, dark region) from the aerogel (0.1 g/cm^3, bright region). The RMI is characterized by a pre-shock Atwood number of $A_0 = (\rho_0 - \rho_1)(\rho_0 + \rho_1) = -0.8$, where ρ_0 is the initial aerogel density and ρ_1 is the initial water density.

Upon the wire array explosion, each individual wire launched a cylindrical shock into its surroundings as visible in Fig. 4 at $t = 0.18\,\mu s$. By $t = 0.88\,\mu s$, the cylindrical shocks had merged to form a stable planar interface propagating at 2.2 ± 0.3 km s^{-1} toward the water–aerogel interface. At impact, numerical simulations suggest that the leading mm of the shock can be modeled as an unsupported planar shock with a variation in the density of $<0.5\%$. A detailed investigation of the formation and planarity of the shock behind the interface produced by this method will be discussed in a separate publication. Due to the planarity of the shock, the compressed water between the wire array and the shock could be characterized by an average post-shock water density of 1.06 ± 0.01 g/cm^3—calculated by considering the difference in the x-ray intensity transmitted through the compressed and

ambient water. Using the measured density jump and shock speed, the pressure behind the planar shockwave in water was estimated via the Rankine–Hugoniot conditions for mass and momentum conservation as $P_{sw} = 300 \pm 100$ MPa, which is significantly larger than the compressive yield strength of the aerogel $Y_{\mathrm{aerogel}} \sim 0.6$ MPa. As such, it is expected that strength effects will not play a significant role and the shock/target interaction will be considered hydrodynamically.

At $t = 1.06\,\mu s$, the shockwave arrived at the minima of the interfacial perturbation, isentropically released to zero pressure, and drove a rarefaction wave back into the water. Shortly after, the shockwave arrived at the maxima, released to zero pressure, and also drove a reflected rarefaction wave. The combined rarefaction waves can be seen in subsequent radiographs ($1.41 < t < 1.58\,\mu s$) as a reflected (bright) wave propagating toward the wires at a speed of 2 ± 0.3 km s^{-1}, where the error on the speed measurement is predominantly due to the uncertainty in the interfacial position measurement. In the regions where the reflected rarefaction waves converged (i.e., focused), we observed a sudden appearance of low-density structures at times $t > 3.87\,\mu s$. The high x-ray transmission through these features is consistent with the formation of cavities within the water volume. These features can be explained by a nucleation of cavitation bubbles in the water, which, unlike gases, can support negative pressures (i.e., tension).[57]

In Fig. 5(a), we show the perturbation amplitude on the interface obtained from the radiographs as a function of laboratory (physical) time t and dimensionless time $t' = [\lambda_0(\lambda_0/2\pi a_0 A\Delta u)]^{-1}t$. The variable t' is present in the scale-free Euler equations, where $(\lambda_0/2\pi a_0 A\Delta u)$ represents the characteristic growth rate of the perturbation predicted by the Richtmyer's impulsive model. In Fig. 5(b), we show the mean position of the interface as a function of laboratory time. The evolution of the interface after shock impact is described by a combination of compressibility effects, linear hydrodynamics, and non-linear hydrodynamic effects. Between $t = 2.9$ and $t = 8.5\,\mu s$, the evolution of the interface perturbation is not shown as its amplitude is close to zero and is hard to distinguish from the compaction wave launched into the aerogel. The time origin $t = 0$ is chosen such that the first radiograph with $t > 0$ captures the wire explosion. Making this choice, the shockwave arrives at the interface perturbation at $t = 1.06\,\mu s$ when the interface is suddenly shock-compressed.

In Fig. 4, between $t = 1.06$ and $t = 1.41\,\mu s$, the shockwave compresses the interface perturbation from $a_0/\lambda = 0.045$ to $a_0/\lambda = 0.034$; an effect visible in Fig. 5(a) as a sudden drop in $a(t)/\lambda$. It is remarkable that the imaging system can resolve the compression phase and does not require any of the assumptions in estimating the post-shock amplitude common for other approaches.[31] After compression, the perturbation continues decreasing in amplitude, passes through zero at $t \sim 5\,\mu s$, and grows in an inverted direction until the end of the measurement.

In an idealized experiment, the dynamics following compression would be asymptotically described by a linear RMI theory if $a(t)/\lambda < 1$ and $t \gg \tau_{\mathrm{ch}}$, where τ_{ch} is a characteristic time required to attain the asymptotic linear solution. In the experiment, the interface develops a non-uniform structure just after impact that appears to be formed by many small vertical jets launched from the water interface into the aerogel (see inset in Fig. 4 at $t = 6.51\,\mu s$). These structures are likely explained by jetting, a strongly non-linear process that occurs due to high-frequency multi-mode perturbations deposited on the aerogel interface during the machining process. Despite being
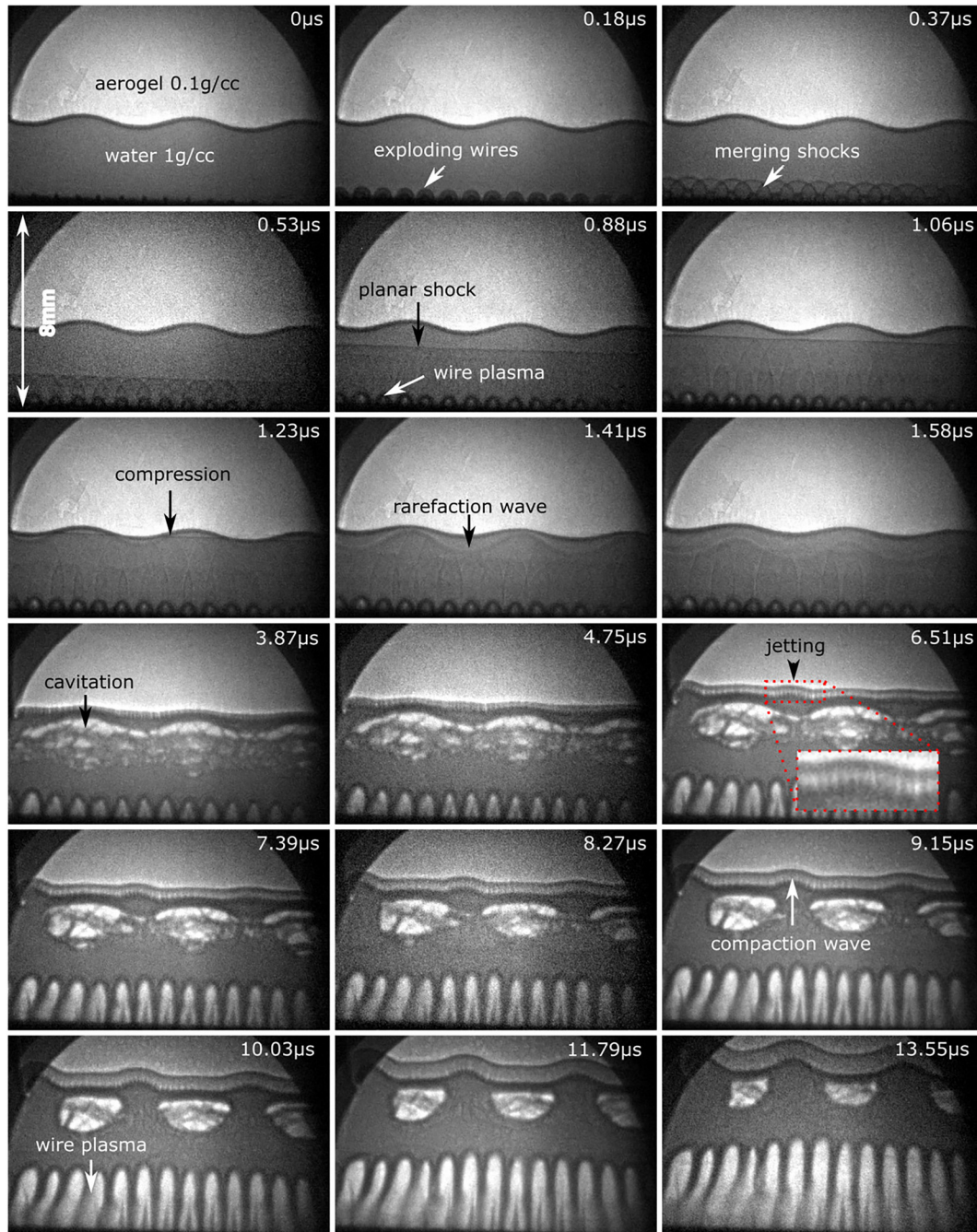
FIG. 4. A selection of x-ray radiographs highlighting the dynamics obtained in a single planar RMI ($A_0 = -0.8$, $a_0/\lambda_0 = 0.045$) experiment. The entire measurement sequence consisted of 256 radiographs spaced 176 ns. Throughout the measurement, the observed intensity corresponds to the line-integrated x-ray transmission through the radiographed material—interpreting darker regions as higher density structures (lower transmission) and brighter regions as lower density structures (higher transmission).

under-resolved, the approximate wavelength of the jets appears to agree with the small perturbations ($\lambda < 400\,\mu$m) seen in the tomograph of the aerogel sample during characterization. Microscopically, these jets are expected to be different even in experiments with the same nominal ICs; however, they should be correctly captured by numerical simulations using the 3D tomograph of the aerogel sample as its ICs. In the following analysis, we will assume that the non-linear processes are small and do not strongly affect the linear growth of the perturbation.
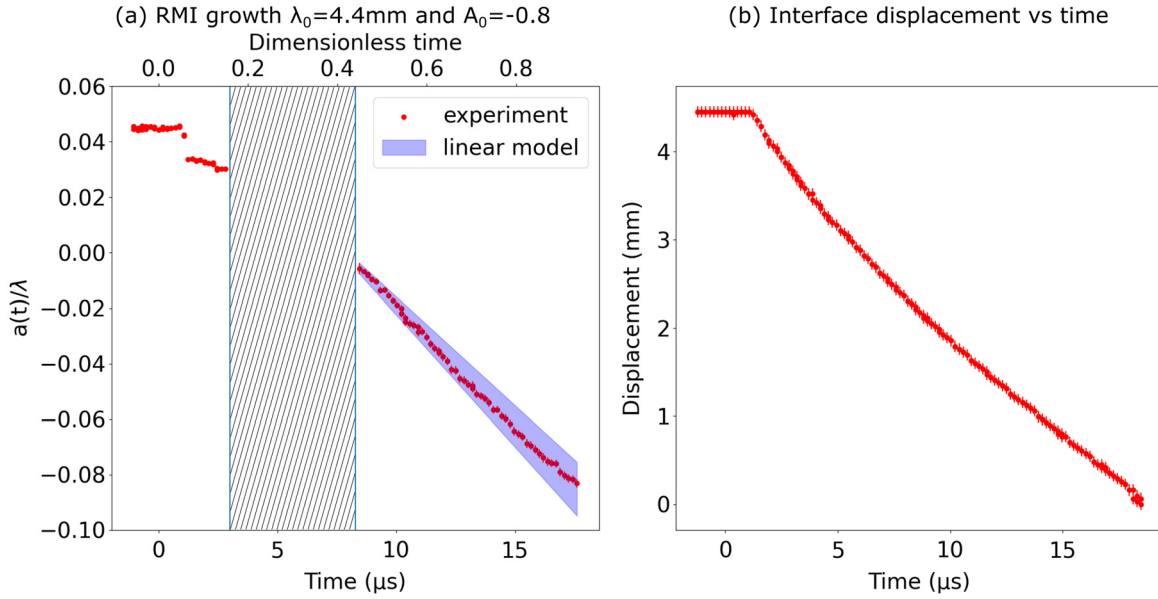
FIG. 5. (a) The red scatter points show the dimensionless interface perturbation amplitude $a(t)/\lambda$ obtained from the radiographs in Fig. 4 as a function of laboratory and dimensionless time. The blue region shows the consistency between the measurement and the linear single-mode RMI theory considering the errors introduced by the interface speed and post-shock density measurement. Between $2.9 < t < 8.5\,\mu s$ (region filled by diagonal stripes) the amplitude is too small to be distinguished from the compaction wave launched into the aerogel. (b) The scatterplot shows the mean position of the interface as a function of time.

As shown in Fig. 5(a), from $t = 8.5\,\mu s$ until the end of the measurement, the growth of the interface perturbation is consistent with the linear RMI theory given by

$$\frac{da(t)}{dt} = ka_0 \Delta u A, \qquad (1)$$

where $a(t)$ is the interface perturbation amplitude, k is the perturbation wavenumber, a_0 is the initial amplitude of the perturbation, Δu is the velocity imparted to the interface by the shock, and A is the Atwood number (pre or post-shock). In our analysis, we use the post-shock Atwood number (between the compressed water and aerogel), and the mean of the pre and the post-shock amplitude is used as a_0. The use of the mean perturbation amplitude before and after compression, instead of the compressed perturbation amplitude, is justified by the work performed by Meyer and Blewett investigating the negative (heavy to light) Atwood number RMI.[58] The estimated values for the interface speed, the post-shock Atwood number, and the compressed amplitude were obtained from the radiographs. During the linear stage, the free interface traveled at $\Delta u = 1.17 \pm 0.01$ km s^{-1}, obtained as a linear fit to Fig. 5(b) between $t = 7.4$ and $t = 16.55\,\mu s$. As the interface propagated forward, it drove a compaction wave through the aerogel moving at 1.24 ± 0.02 km s^{-1}. As a result, the aerogel was compressed from 0.1 ± 0.02 to 0.18 ± 0.05 g/cm^3 as measured by the mean x-ray transmission. As such, the post-shock Atwood number A_1 was equal to -0.7 ± 0.1. Furthermore, the Fourier transform of the interface perturbation shows a single dominant wavelength $\lambda \sim 4.4$ mm throughout the growth of the RMI ($t > 7.4\,\mu s$), confirming that the entire measurement is within the linear regime where the above theory should be applicable.

At the beginning of the RMI growth, between $t = 1.1$ and $t = 3.1\,\mu s$, the measured growth speed of the perturbation was not constant and did not appear to follow the asymptotic linear theory. This effect can be explained by the proximity of the compaction wave to the perturbation effectively decreasing the RMI growth rate.[5] In the small amplitude theory, the RMI instability initially accelerates from $da(t)/dt = 0$ to reach the asymptotic limit at $t \gg \tau_{ch}$, where τ_{ch} represents a characteristic time over which the presence of reflected and transmitted shocks affects the instability growth. For the heavy–light configuration, the characteristic time τ_{ch} is given by $\tau_{ch} = (\lambda_0/4\pi)[(1 - A^+)/U_1 + (1 + A^+)/U_2]$, where U_1 is the speed of the reflected shock and U_2 is the speed of the transmitted shock.[59] Substituting the shock speeds for the transmitted compaction wave and reflected rarefaction wave speeds, the characteristic time for the measured experiment is $\tau_{ch} \sim 2\,\mu s$. This estimate is consistent with the experiment reaching the asymptotic linear growth speed by $t \sim 8\,\mu s$, despite being at an early dimensionless time t'.

Finally, in Fig. 6(a), we present an alternative experimental design highlighting the multi-geometry capability of our approach. In this instance, the wire array consisted of 19 copper wires of $64\,\mu m$ diameter equally distributed on a cylindrical surface of 7 mm radius. Previous experiments showed that cylindrical wire explosion can drive inward—propagating converging cylindrical shocks in water at speeds > 4.5 km s^{-1}. In this experiment, the wires were encapsulated in gelatin (3% concentration, $\rho_0 = 1$ g/cm^3) with yield strength $Y \sim 10$ kPa.[60] The gelatin contained a hollow region in its center with pre-imposed azimuthal perturbations. Parametrically, the boundary of the hollow region could be described by

$$x_t = (r_0 + a_0 \sin(16\phi))\cos(\phi), \qquad (2)$$

$$y_t = (r_0 + a_0 \sin(16\phi))\sin(\phi), \qquad (3)$$
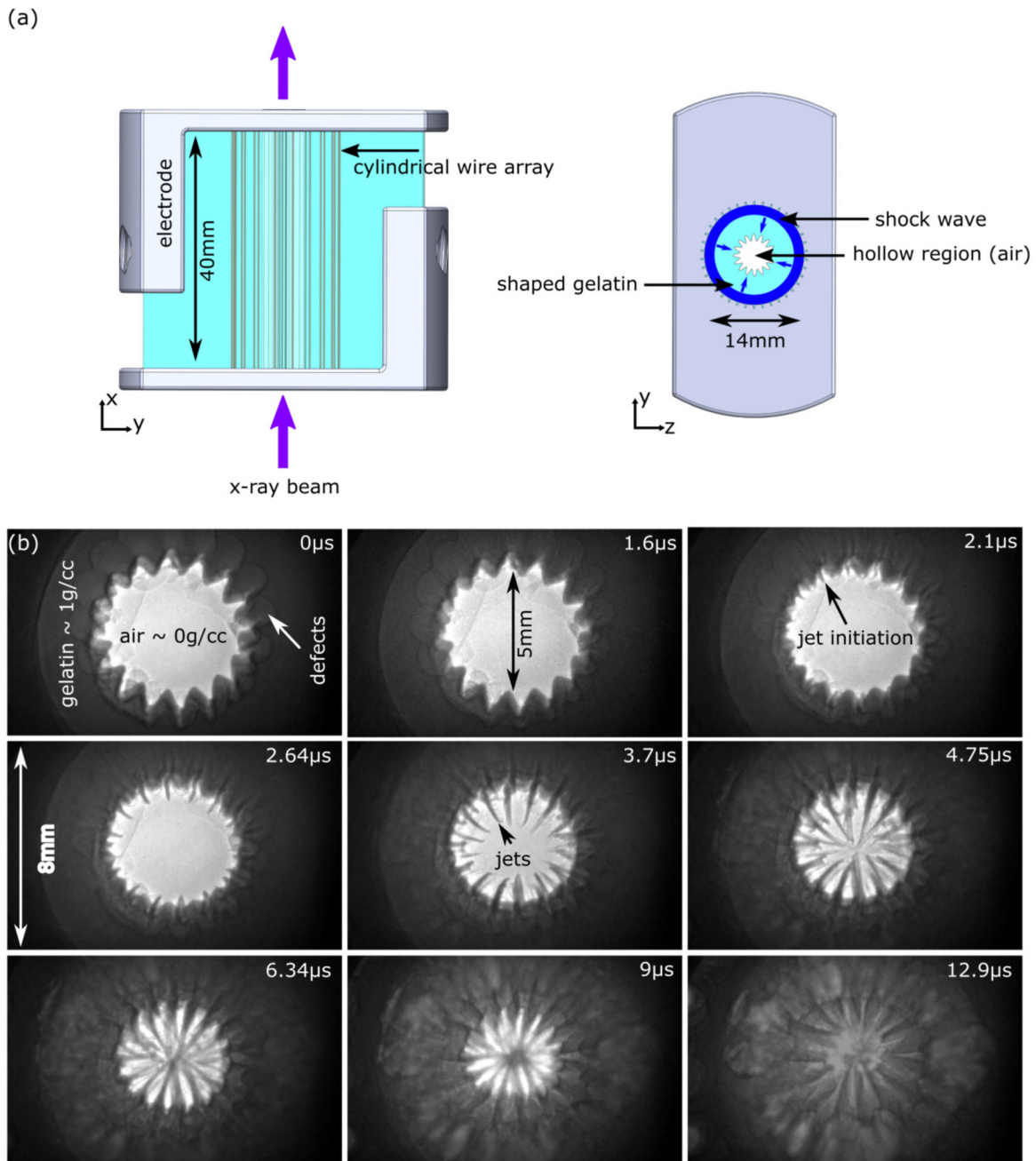
FIG. 6. (a) An example design of a non-planar RMI experiment using the exploding wire technique. The wire array forms a cylindrical shell that will drive a cylindrically converging shock onto the target located on axis. (b) A selection of preliminary radiographs obtained by performing the cylindrical RMI experiment shown in Fig. 6(b) (16-mode perturbation, $a_0/\lambda_0 \sim 1$). The axial jets are visible with high contrast due to their axial correlation along the line-of-sight.

where (x_t, y_t) are the cartesian coordinates defined for angles $\phi \in [0, 2\pi)$, $r_0 = 2.5$ mm and $a_0 = 0.5$ mm. In this geometry, the wavelength λ_0 of the pre-imposed perturbation was approximately equal to its initial amplitude a_0, and the initial amplitude was comparable to the total radius r_0. As such, it is expected that the interface

dynamics following a shock impact become non-linear and exhibit convergent effects. In Fig. 6(b), we show preliminary results of such an experimental investigation, where the RMI is characterized by an Atwood number of $A = -1$. In these radiographs, the exploding wires cannot be observed as they are located outside of the field of view—

7 mm from the center of the target. At $t = 0\,\mu s$, it is possible to see large-scale defects associated with the manufacturing of the target as well as tip-tilt errors inherent in probing an extended cylindrical object. At $t = 1.6\,\mu s$, the cylindrically convergent shock impacts the gelatin–air interface and initiates the subsequent RMI growth. By $t = 2.64\,\mu s$, the RMI growth is characterized by a strong jetting behavior, whereas the usual "bubble" and "spike" growth is strongly asymmetric and leads to a central collision and accumulation of mass transported by the jetting phenomenon.

V. CONCLUSIONS

In this article, we presented a novel, shape-agnostic, membraneless approach to shock-driven hydrodynamic experiments involving a combination of a pulsed power driven electrical wire explosion to drive high pressure shockwaves in water ($P > 100\,MPa$) and synchrotron multi-frame x-ray imaging diagnostic. The technique offers a number of advantages, including the ability to shape the experimental geometry, produce high pressures that enable the use of liquid and solid materials as hydrodynamic targets, and co-time the experiment with multi-MHz radiography to acquire all data within a single experiment, eliminating uncertainties regarding repeatability of the ICs.

Currently, the synchrotron x-ray diagnostic at the European Synchrotron Radiation Facility ID19 can acquire up to 256 radiographs, spaced 176 ns apart, and with an exposure time of 60ps on each experiment. The spatial resolution each radiograph is $32\,\mu m/pixel$ with the field-of-view spanning $8 \times 12.8\,mm^2$ (V × H). This resolution can be increased up to $3.2\,\mu m/pixel$ at the cost of proportional decrease in the field-of-view. These characteristics make this approach a valuable diagnostic for single-experiment, multi-frame measurements—especially in the late nonlinear development of hydrodynamic instabilities where the knowledge and the repeatability of the ICs may play a significant role.

To establish this technique, we conducted a small amplitude planar RMI experiment at the ESRF. As this type of experiment has a well-established theory with abundant experimental evidence, it serves as a good point-of-comparison against other hydrodynamic platforms. In the experiment, a planar shockwave propagating in water at $2.2 \pm 0.3\,km\,s^{-1}$ was driven by an underwater wire array explosion produced by a $\sim 30\,kA$ discharge in $\sim 1000\,ns$. The shockwave impacted a sinusoidal perturbation on a water–aerogel interface characterized by a pre-shock Atwood number of $A_0 = -0.8$. Radiography of the subsequent dynamics obtained a very highly resolved RMI growth, including the period of perturbation compression, compaction wave detachment, and linear RMI growth. Shortly after the shock impact, the perturbation growth did not agree with the asymptotic linear RMI theory due to the proximity of the compaction wave (in the aerogel sample) to the perturbation. When the compaction wave propagated sufficiently far, but the interface perturbation still satisfied the linear RMI criterion, it was shown that the growth of the interface was consistent with the asymptotic linear theory. The agreement suggests that this approach can capture purely hydrodynamic phenomena using liquid and solid materials; however, the consistency between the shown experiments and the small amplitude RMI theory does not guarantee ideal hydrodynamic behavior in the nonlinear stage. Importantly, the temporal resolution of the measurement was sufficient to capture the compression of the perturbation during the shock impact and so did not require any assumptions to estimate the post-

shock perturbation amplitude. The x-ray radiography also unveiled other related phenomena that could be investigated, such as cavitation in liquids caused by converging rarefaction waves.

In the future, we aim to use this technique to explore the nonlinear growth of the RMI with well-characterized initial conditions in both planar and cylindrical geometries. To extend the measurement into the nonlinear regime, the ICs can be adjusted by decreasing the perturbation wavelength λ_0 and increasing the time between radiographs. These changes should allow the experiment to capture a larger range of the dimensionless instability evolution. It is also possible to initiate the experiments in the regime, where $a_0/\lambda_0 \sim 1$ to obtain significant velocity shear, thus initiating the growth of the Kelvin–Helmholtz instability and amplified fluid-mixing early in the experiment. To diagnose the nonlinear experiments, it is necessary to improve the on-shot characterization of the x-ray source or use a monochromatic source, such as an x-ray free-electron laser to directly measure the mass mixing fraction during the experiment—a metric that is much more suitable for the characterization of the nonlinear mixing stage than the usually measured instability amplitude (mixing zone width).[61] Due to the versatility of this approach, other experiments are also possible, including but not limited to, thin-layer RMI experiments or experiments involving multiply re-shocked interfaces.

AUTHOR DECLARATIONS
Conflict of Interest

The authors have no conflicts to disclose.

Author Contributions

Jergus Strucka: Conceptualization (lead); Data curation (equal); Formal analysis (lead); Investigation (equal); Methodology (lead); Writing – original draft (equal). **Alexander Rack:** Supervision (equal); Writing – review & editing (equal). **Yakov E. Krasik:** Investigation (equal); Resources (equal); Supervision (equal); Writing – review & editing (equal). **Jeremy P. Chittenden:** Conceptualization (equal); Supervision (equal); Writing – review & editing (equal). **Simon N. Bland:** Conceptualization (equal); Data curation (equal); Investigation (equal); Project administration (equal); Resources (equal); Supervision (lead); Writing – review & editing (equal). **Bratislav Lukic:** Investigation (equal); Writing – review & editing (equal). **Marlene Koerner:** Formal analysis (equal). **Jack W. D. Halliday:** Supervision (equal); Writing – review & editing (equal). **Yifan Yao:** Investigation (supporting). **Kassim Mughal:** Investigation (supporting). **Daniel Maler:** Investigation (supporting). **Sergey Efimov:** Investigation (supporting). **J. Skidmore:** Resources (equal); Supervision (equal); Writing – review & editing (equal).

DATA AVAILABILITY

The data that support the findings of this study are available from the corresponding author upon reasonable request.

REFERENCES

[1] J. Matsumoto and Y. Masada, "Rayleigh-Taylor and Richtmyer-Meshkov instabilities in relativistic hydrodynamic jets," EPJ Web Conf. **61**, 02005 (2013).

[2] J. Kane, R. P. Drake, and B. A. Remington, "An evaluation of the Richtmyer-Meshkov instability in supernova remnant formation," Astrophys. J. **511**, 335 (1999).

[3] A. Ravid, R. I. Citron, and R. Jeanloz, "Hydrodynamic instability at impact interfaces and planetary implications," Nat. Commun. **12**, 2104 (2021).

[4] S. W. Haan, J. D. Lindl, D. A. Callahan, D. S. Clark, J. D. Salmonson, B. A. Hammel, L. J. Atherton, R. C. Cook, M. J. Edwards, S. Glenzer, A. V. Hamza, S. P. Hatchett, M. C. Herrmann, D. E. Hinkel, D. D. Ho, H. Huang, O. S. Jones, J. Kline, G. Kyrala, O. L. Landen, B. J. MacGowan, M. M. Marinak, D. D. Meyerhofer, J. L. Milovich, K. A. Moreno, E. I. Moses, D. H. Munro, A. Nikroo, R. E. Olson, K. Peterson, S. M. Pollaine, J. E. Ralph, H. F. Robey, B. K. Spears, P. T. Springer, L. J. Suter, C. A. Thomas, R. P. Town, R. Vesey, S. V. Weber, H. L. Wilkens, and D. C. Wilson, "Point design targets, specifications, and requirements for the 2010 ignition campaign on the National Ignition Facility," Phys. Plasmas **18**, 051001 (2011).

[5] Y. Zhou, "Rayleigh–Taylor and Richtmyer–Meshkov instability induced flow, turbulence, and mixing. I," Phys. Rep. **720–722**, 1–136 (2017).

[6] Y. Zhou, "Rayleigh–Taylor and Richtmyer–Meshkov instability induced flow, turbulence, and mixing. II," Phys. Rep. **723–725**, 1–160 (2017).

[7] Y. Zhou, T. T. Clark, D. S. Clark, S. G. Glendinning, M. A. Skinner, C. M. Huntington, O. A. Hurricane, A. M. Dimits, and B. A. Remington, "Turbulent mixing and transition criteria of flows induced by hydrodynamic instabilities," Phys. Plasmas **26**, 080901 (2019).

[8] Y. Zhou, R. J. Williams, P. Ramaprabhu, M. Groom, B. Thornber, A. Hillier, W. Mostert, B. Rollin, S. Balachandar, P. D. Powell, A. Mahalov, and N. Attal, "Rayleigh–Taylor and Richtmyer–Meshkov instabilities: A journey through scales," Physica D **423**, 132838 (2021).

[9] K. O. Mikaelian, "Richtmyer–Meshkov instability of arbitrary shapes," Phys. Fluids **17**, 034101 (2005).

[10] M. Fan, Z. Zhai, T. Si, X. Luo, L. Zou, and D. Tan, "Numerical study on the evolution of the shock-accelerated SF_6 interface: Influence of the interface shape," Sci. China **55**, 284–296 (2012).

[11] D. M. Sterbentz, C. F. Jekel, D. A. White, S. Aubry, H. E. Lorenzana, and J. L. Belof, "Design optimization for Richtmyer–Meshkov instability suppression at shock-compressed material interfaces," Phys. Fluids **34**, 082109 (2022).

[12] M. Groom and B. Thornber, "The influence of initial perturbation power spectra on the growth of a turbulent mixing layer induced by Richtmyer–Meshkov instability," Physica D **407**, 132463 (2020).

[13] B. Thornber, D. Drikakis, D. L. Youngs, and R. J. R. Williams, "The influence of initial conditions on turbulent mixing due to Richtmyer–Meshkov instability," J. Fluid Mech. **654**, 99–139 (2010).

[14] M. L. Wong, D. Livescu, and S. K. Lele, "High-resolution Navier-Stokes simulations of Richtmyer-Meshkov instability with reshock," Phys. Rev. Fluids **4**, 104609 (2019).

[15] M. Mohaghar, J. McFarland, and D. Ranjan, "Three-dimensional simulations of reshocked inclined Richtmyer-Meshkov instability: Effects of initial perturbations," Phys. Rev. Fluids **7**, 093902 (2022).

[16] K. R. Bates, N. Nikiforakis, and D. Holder, "Richtmyer-meshkov instability induced by the interaction of a shock wave with a rectangular block of SF_6," Phys. Fluids **19**, 036101 (2007).

[17] J. Bai, L. Zou, T. Wang, K. Liu, W. Huang, J. Liu, P. Li, D. Tan, and C. Liu, "Experimental and numerical study of shock-accelerated elliptic heavy gas cylinders," Phys. Rev. E **82**, 056318 (2010).

[18] L. Zou, W. Huang, C. Liu, J. Yu, and X. Luo, "On the evolution of double shock-accelerated elliptic gas cylinders," J. Fluids Eng. **136**, 091205 (2014).

[19] J. McFarland, D. Reilly, S. Creel, C. McDonald, T. Finn, and D. Ranjan, "Experimental investigation of the inclined interface Richtmyer–Meshkov instability before and after reshock," Exp. Fluids **55**, 1640 (2013).

[20] X. Luo, P. Dong, T. Si, and Z. Zhai, "The Richtmyer–Meshkov instability of a 'v' shaped air/interface," J. Fluid Mech. **802**, 186–202 (2016).

[21] Z. Zhai, P. Dong, T. Si, and X. Luo, "The Richtmyer-Meshkov instability of a 'v' shaped air/helium interface subjected to a weak shock," Phys. Fluids **28**, 082104 (2016).

[22] D. Reilly, J. McFarland, M. Mohaghar, and D. Ranjan, "The effects of initial conditions and circulation deposition on the inclined-interface reshocked Richtmyer–Meshkov instability," Exp. Fluids **56**, 168 (2015).

[23] S. Balasubramanian, G. C. Orlicz, and K. P. Prestridge, "Experimental study of initial condition dependence on turbulent mixing in shock-accelerated Richtmyer–Meshkov fluid layers," J. Turbul. **14**, 170–196 (2013).

[24] M. A. Jones and J. W. Jacobs, "A membraneless experiment for the study of Richtmyer–Meshkov instability of a shock-accelerated gas interface," Phys. Fluids **9**, 3078–3085 (1997).

[25] R. D. Richtmyer, "Taylor instability in shock acceleration of compressible fluids," Commun. Pure Appl. Math. **13**, 297–319 (1960).

[26] R. V. Morgan, O. A. Likhachev, and J. W. Jacobs, "Rarefaction-driven rayleigh–taylor instability. part 1. diffuse-interface linear stability measurements and theory," J. Fluid Mech. **791**, 34–60 (2016).

[27] C. R. Weber, N. S. Haehn, J. G. Oakley, D. A. Rothamer, and R. Bonazza, "An experimental investigation of the turbulent mixing transition in the Richtmyer–Meshkov instability," J. Fluid Mech. **748**, 457–487 (2014).

[28] M. Mohaghar, J. Carter, B. Musci, D. Reilly, J. McFarland, and D. Ranjan, "Evaluation of turbulent mixing transition in a shock-driven variable-density flow," J. Fluid Mech. **831**, 779–825 (2017).

[29] M. Mohaghar, J. Carter, G. Pathikonda, and D. Ranjan, "The transition to turbulence in shock-driven mixing: Effects of Mach number and initial conditions," J. Fluid Mech. **871**, 595–635 (2019).

[30] J. Sauppe, S. Palaniyappan, B. Tobias, J. Kline, K. Flippo, O. Landen, D. Shvarts, S. Batha, P. Bradley, E. Loomis, N. Vazirani, C. Kawaguchi, L. Kot, D. Schmidt, T. Day, A. Zylstra, and E. Malka, "Demonstration of scale-invariant Rayleigh-Taylor instability growth in laser-driven cylindrical implosion experiments," Phys. Rev. Lett. **124**, 185003 (2020).

[31] P. F. Knapp, M. R. Martin, D. Yager-Elorriaga, A. J. Porwitzky, F. W. Doss, G. A. Shipley, C. A. Jennings, D. E. Ruiz, T. Byvank, C. C. Kuranz, C. E. Myers, D. H. Dolan, K. Cochrane, M. Schollmeier, I. C. Smith, T. R. Mattsson, B. M. Jones, K. Peterson, J. Schwarz, R. D. McBride, D. G. Flicker, and D. B. Sinars, "A novel, magnetically driven convergent Richtmyer–Meshkov platform," Phys. Plasmas **27**, 092707 (2020).

[32] G. Rigon, B. Albertazzi, P. Mabey, T. Michel, E. Falize, V. Bouffetier, L. Ceurvorst, L. Masse, M. Koenig, and A. Casner, "Exploring the Atwood-number dependence of the highly nonlinear Rayleigh-Taylor instability regime in high-energy-density conditions," Phys. Rev. E **104**, 045213 (2021).

[33] T. Desjardins, C. D. Stefano, T. Day, D. Schmidt, E. Merritt, F. Doss, K. Flippo, T. Cardenas, B. DeVolder, P. Donovan, S. Edwards, F. Fierro, R. Gonzales, L. Goodwin, C. Hamilton, T. Quintana, R. Randolph, A. Rasmus, T. Sedillo, C. Wilson, and L. Welser-Sherrill, "A platform for thin-layer Richtmyer-Meshkov at OMEGA and the NIF," High Energy Density Phys. **33**, 100705 (2019).

[34] Y. E. Krasik, A. Fedotov, D. Sheftman, S. Efimov, A. Sayapin, V. T. Gurovich, D. Veksler, G. Bazalitski, S. Gleizer, A. Grinenko, and V. I. Oreshkin, "Underwater electrical wire explosion," Plasma Sources Sci. Technol. **19**, 034020 (2010).

[35] H. Shi, G. Yin, X. Li, J. Wu, A. B. Murphy, Y. Zhang, and A. Qiu, "Electrical wire explosion as a source of underwater shock waves," J. Phys. D **54**, 403001 (2021).

[36] D. Maler, S. Efimov, M. Liverts, S. Theocharous, J. Strucka, Y. Yao, W. Proud, A. Rack, B. Lukic, S. N. Bland, and Y. E. Krasik, "Peculiarities of planar shock-wave interaction with air–water interface and solid target," Phys. Plasmas **29**, 063502 (2022).

[37] S. Efimov, V. T. Gurovich, G. Bazalitski, A. Fedotov, and Y. E. Krasik, "Addressing the efficiency of the energy transfer to the water flow by underwater electrical wire explosion," J. Appl. Phys. **106**, 073308 (2009).

[38] S. N. Bland, Y. E. Krasik, D. Yanuka, R. Gardner, J. MacDonald, A. Virozub, S. Efimov, S. Gleizer, and N. Chaturvedi, "Generation of highly symmetric, cylindrically convergent shockwaves in water," Phys. Plasmas **24**, 082702 (2017).

[39] L. Li, D. Qian, X. Zou, and X. Wang, "Underwater electrical wire explosion: Shock wave from melting being overtaken by shock wave from vaporization," Phys. Plasmas **25**, 053502 (2018).

[40] O. Antonov, S. Efimov, D. Yanuka, M. Kozlov, V. T. Gurovich, and Y. E. Krasik, "Generation of converging strong shock wave formed by microsecond timescale underwater electrical explosion of spherical wire array," Appl. Phys. Lett. **102**, 124104 (2013).

[41]D. Yanuka, S. Theocharous, and S. N. Bland, "Pulsed power driven cylindrical wire array explosions in different media," Phys. Plasmas **26**, 122704 (2019).

[42]S. Sembian, M. Liverts, N. Tillmark, and N. Apazidis, "Plane shock wave interaction with a cylindrical water column," Phys. Fluids **28**, 056102 (2016).

[43]R. Han, J. Wu, H. Zhou, Y. Zhang, A. Qiu, J. Yan, W. Ding, C. Li, C. Zhang, and J. Ouyang, "Experiments on the characteristics of underwater electrical wire explosions for reservoir stimulation," Matter Radiat. Extremes **5**, 047201 (2020).

[44]S. P. Theocharous, S. N. Bland, D. Yanuka, A. Rososhek, M. P. Olbinado, A. Rack, and Y. E. Krasik, "Use of synchrotron-based radiography to diagnose pulsed power driven wire explosion experiments," Rev. Sci. Instrum. **90**, 013504 (2019).

[45]D. Maler, M. Liverts, S. Efimov, A. Virozub, and Y. E. Krasik, "Addressing the critical parameters for overdamped underwater electrical explosion of wire," Phys. Plasmas **29**, 102703 (2022).

[46]V. I. Oreshkin and R. B. Baksht, "Wire explosion in vacuum," IEEE Trans. Plasma Sci. **48**, 1214–1248 (2020).

[47]S. W. Wilkins, T. E. Gureyev, D. Gao, A. Pogany, and A. W. Stevenson, "Phase-contrast imaging using polychromatic hard x-rays," Nature **384**, 335–338 (1996).

[48]M. P. Olbinado, X. Just, J.-L. Gelet, P. Lhuissier, M. Scheel, P. Vagovic, T. Sato, R. Graceffa, J. Schulz, A. Mancuso, J. Morse, and A. Rack, "MHz frame rate hard x-ray phase-contrast imaging using synchrotron radiation," Opt. Express **25**, 13857 (2017).

[49]M. P. Olbinado, V. Cantelli, O. Mathon, S. Pascarelli, J. Grenzer, A. Pelka, M. Roedel, I. Prencipe, A. L. Garcia, U. Helbig, D. Kraus, U. Schramm, T. Cowan, M. Scheel, P. Pradel, T. D. Resseguier, and A. Rack, "Ultra high-speed x-ray imaging of laser-driven shock compression using synchrotron light," J. Phys. D **51**, 055601 (2018).

[50]E. M. Escauriza, M. P. Olbinado, M. E. Rutherford, D. J. Chapman, J. C. Z. Jonsson, A. Rack, and D. E. Eakins, "Ultra-high-speed indirect x-ray imaging system with versatile spatiotemporal sampling capabilities," Appl. Opt. **57**, 5004 (2018).

[51]P. A. Douissard, A. Cecilia, X. Rochet, X. Chapel, T. Martin, T. van de Kamp, L. Helfen, T. Baumbach, L. Luquot, X. Xiao, J. Meinhardt, and A. Rack, "A versatile indirect detector design for hard x-ray microimaging," J. Instrumentation **7**, P09016 (2012).

[52]T. D. Aslam, R. L. Gustavsen, and B. D. Bartram, "An equation of state for polyurea aerogel based on multi-shock response," J. Phys.: Conf. Ser. **500**, 032001 (2014).

[53]N. Whitworth and B. Lambourn, "A single-phase analytic equation of state for solid polyurea and polyurea aerogels," AIP Conf. Proc. **1979**, 030007 (2018).

[54]J. E. Gorfain, C. T. Key, D. Veysset, and K. A. Nelson, "Simulation of polyurea shock response under high-velocity microparticle impact," AIP Conf. Proc. **1979**, 090005 (2018).

[55]D. Paganin, S. C. Mayo, T. E. Gureyev, P. R. Miller, and S. W. Wilkins, "Simultaneous phase and amplitude extraction from a single defocused image of a homogeneous object," J. Microscopy **206**, 33–40 (2002).

[56]H. Payno, P. Paleo, C. Nemoz, P. Cloetens, M. di Michiel, A. Rack, P. Tafforeau, V. A. Solé, and N. R. Viganò, "Overcoming the data processing challenges of unifying tomography techniques at ESRF," J. Phys.: Conf. Ser. **2380**, 012106 (2022).

[57]F. Caupin, "Liquid-vapor interface, cavitation, and the phase diagram of water," Phys. Rev. E **71**, 051605 (2005).

[58]K. A. Meyer, "Numerical investigation of the stability of a shock-accelerated interface between two fluids," Phys. Fluids **15**, 753 (1972).

[59]M. Lombardini, "Richtmyer-Meshkov instability in converging geometries," Ph.D. thesis (California Institute of Technology, 2008).

[60]S. Bakhrakh, O. Drennov, and N. Kovalev, "Hydrodynamic instability in strong media," Report No. UCRL-CR-126710 published under LLNL-VNIIEF (Lawrence Livermore National Lab., 1997), https://www.osti.gov/biblio/515973.

[61]Y. Zhou, W. H. Cabot, and B. Thornber, "Asymptotic behavior of the mixed mass in Rayleigh–Taylor and Richtmyer–Meshkov instability induced flows," Phys. Plasmas **23**, 052712 (2016).

[62]See http://www.buyaerogel.com/product/airloy-x103/ for Airloy® X103 Strong Aerogel Tiles.

11 September 2023 06:30:17